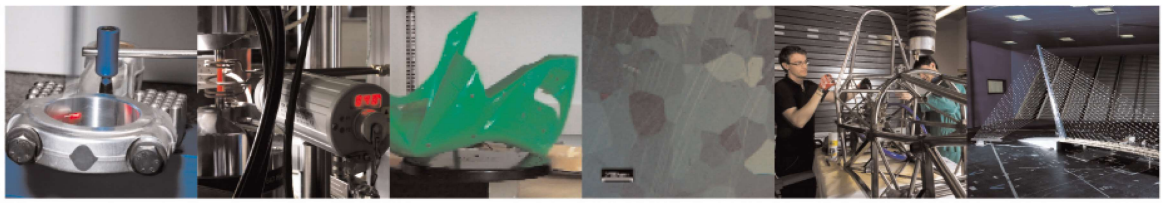

Numerical simulation of particles flow in Laser Metal Deposition technology comparing Eulerian-Eulerian and Lagrangian-Eulerian approaches

Murer, M.; Furlan, V.; Formica, G.; Morganti, S.; Previtali, B.; Auricchio, F.

This is a post-peer-review, pre-copyedit version of an article published in JOURNAL OF MANUFACTURING PROCESSES. The final authenticated version is available online at: http://dx.doi.org/10.1016/j.jmapro.2021.05.027

Numerical simulation of particles flow in Laser Metal Deposition technology comparing Eulerian-Eulerian and Lagrangian-Eulerian approaches

Mauro Murer[a,*], Valentina Furlan[d], Giovanni Formica[b], Simone Morganti[c], Barbara Previtali[d], Ferdinando Auricchio[a]

[a]*Dipartimento di Ingegneria Civile e Architettura, Università di Pavia, Pavia, Italy*
[b]*Dipartimento di Architettura, Università degli Studi Roma Tre, Roma, Italy*
[c]*Dipartimento di Ingegneria Industriale e dell'Informazione, Università di Pavia, Pavia, Italy*
[d]*Dipartimento di Meccanica, Politecnico di Milano, Milano, Italy*

Abstract

The present work deals with the numerical prediction of the particle flow within a three-way nozzle in Laser Metal Deposition (LMD) technology adopted during additive manufacturing processes. In particular, the paper focuses on CFD (Computational Fluid Dynamics) simulations of the particle flow problem, regarding the coupling between a fluid phase, *i.e.*, the carrier gas, and a solid phase, *i.e.*, a metallic material powder that is delivered through the nozzle of the LMD machine.

Two different numerical approaches are investigated, both implemented in a in-house code using OpenFOAM open source C++ toolbox. The former is based on a mixed formulation, combining an Eulerian description of the carrier gas flow with a Lagrangian description of the particle flow. The latter on a pure Eulerian formulation of both carrier gas and particles.

In agreement with the experimental evidences, the present work compares the two approaches in terms of capability of simulating some key physical features of the LMD process, *i.e.*, the geometrical properties of the powder cone formed out from the nozzle.

Keywords: powder flow simulation, three-way nozzle, eulerian method, lagrangian

*Corresponding author
Email addresses: mauro.murer01@universitadipavia.it (Mauro Murer), valentina.furlan@polimi.it (Valentina Furlan), formica@uniroma3.it (Giovanni Formica), simone.morganti@unipv.it (Simone Morganti), barbara.previtali@polimi.it (Barbara Previtali), auricchi@unipv.it (Ferdinando Auricchio)

method, laser metal deposition

1. Introduction

Additive Manufacturing (AM) refers to an engineering process in which objects are built up and then fabricated by means of adding, melting, and solidifying material (typically powder or wire) layer by layer, opposed to the subtractive technologies [1]. Such a process is particularly appropriate to produce complex and near-net shape geometries due to its high flexibility especially in terms of design. Among several categories of AM processes, Direct Energy Deposition (DED) is suitable for producing metal parts via a local (direct) layer by layer deposition of molten metal materials, with a simultaneous delivery of beam and raw material. More in general, DED processes are based on the heating and melting of a substrate due to a direct energy source, as well as the simultaneous melting of raw material (powder or wire) that is deposited on the substrate. In contrast with techniques of powder bed fusion which melt a material that is prelaid in a powder bed, DED processes melt materials as they are being deposited in the so-called melt pool [2]. Depending on the thermal energy source, DED can be distinguished in Electron Beam Metal Deposition (EBMD), Plasma Metal Deposition (PMD), and Laser Metal Deposition (LMD). The present work focuses on this latter.

LMD emerged in the modern industry (*e.g.*, aeronautics, automotive, biomedics) as one of the most important manufacturing technology, due its capability of producing complex geometries and light-weight components, repairing damaged components, creating coatings and depositing multi-material and functionally-graded compositions [3, 4]. Taking into account economical aspects, the LMD technology is attractive especially in terms of design flexibility and capability in reducing component weight, as well as in saving time and energy throughout the fabrication process. Material waste and its recycle may be also considered from a sustainability viewpoint [5].

Due to its nature, LMD is inherently a multi-physics process involving particle transportation, multiple flow interaction, particles-gas interaction with energy source and material phase-change (from solid powder to liquid phase and then a solidification again). The LMD process can be conveniently simplified in three different physical

phenomena: (i) particles flow inside and outside the nozzle; (ii) interaction between laser beam and moving powders; (iii) particle deposition, fusion and solidification inside the melt pool, partially composed by molten substrate/layer material. The present work focuses only on the first one, and numerical issues regarding the prediction of the particles flow and the design optimization of the coaxial nozzle are tackled. The investigation of the particle flow inside and outside the three-way nozzle is propaedeutic for the correct prediction of the phenomenon, since the powder delivery at the exit of the nozzle strongly affects the entire process. The powder flow rate is directly connected to different factors, which are able to change the geometrical shape of the cone and its main properties like the waist diameter of the powder and its position. Powder cone alterations are able to produce a different behavior in terms of material processability. In this perspective, the simulation of powder delivery up to the nozzle is mandatory to control the process.

Concerning the numerical methods able to predict the particle flow, the Lagrangian approach is one of the most commonly used in the literature, due to its ability to work as particle-tracking method. One of the early work was done by Pan and Liou [6] who developed a stochastic model that accounts for particle shape effects, in particular non-spherical collisions through stochastic parameters, and that is able to quickly simulate realistic powder flow. Once validated with experiments, such a model allows the authors to evaluate various nozzle geometrical configurations, showing the dispersion of metallic powder due to the deviation from the sphere-shape in particle morphology. Such a dispersion evolution plays a key role in the focusability of the powder stream and powder spatial concentration, and it turns out that width and outer diameter of the powder outlet passage are important dimensions in the determination of the powder stream structure. The same authors improved the stochastic model in a subsequent work [7], where effects of outer shielding gas directions and inner/outer shielding gas flow rate had been also considered in the model. Zhang et al. [8] conducted a comprehensive numerical study that investigates the effect of pressure and nozzle dimension on particle distribution and velocity in laser cladding systems. They developed three-dimensional CFD models in ANSYS-FLUENT, solved using a Discrete Phase Modeling (DPM) approach to compute particles acceleration while Navier-Stokes equa-

tions have been considered to model the inert gas. In particular the authors found out that during laser cladding processes higher particle velocity and more compact powder flow can be obtained by Helium vacuum environment than using Argon. Along the same research perspective, similar approaches aiming at optimizing nozzle design and validating particle flow experimental measurements can be previously found in [9, 10]. Also [11, 12, 13] have developed numerical strategies based on CFD coupled with particle-tracking methods to explore how nozzle geometry, powder properties, and feeding parameters can improve LMD process efficiency.

The last mentioned methods can be framed in a so called Lagrangian-Eulerian formulation – sometimes indicated as CFD-DEM (Computational Fluid Dynamics - Discrete Element Method) – where a Lagrangian approach for the particles solution is effectively combined with an Eulerian one that is used for the flow solution. An alternative formulation consists of a pure Eulerian framework, namely Eulerian-Eulerian model, where both particles and flow are treated as Eulerian fluids. While the former approach has been extensively adopted, the latter has never been considered for simulating LMD processes. Computational advantages/disadvantage of both the approaches have been explored only in different application fields. To cite a few, we mention turbulent dispersion and coalescence of droplets within a spray [14], particle-laden flows subject to radiative heating [15], and fluidized bed systems [16].

In [14] both Lagrangian and Eulerian approaches proved to be able to simulate droplet turbulent dispersion and coalescence for a wide range of droplet and gas flows, and for sprays from nozzles that produce different droplet-size distributions. Also the computational time was found to be of similar orders of magnitude, regardless of which formulation, Eulerian or Lagrangian, is adopted. Yet, in the Eulerian formulation droplet-size class is represented as a continuum with a single velocity at any point in space, thus limiting wider range of solutions in terms of droplet-size distribution that Langrangian simulations offer. Similar results were observed in [15], where an Eulerian moment method was developed as alternative to Lagrangian particle tracking for solving the disperse phase statistics in thermally two-way coupled system. The Eulerian method, although reproducing accurately equivalent gas phase obtained through Langrangian simulations, cannot capture more than one velocity per position, and then

proves to be not valid when particle trajectory crossing occurs. Finally, in [16] both the Lagrangian and Eulerian approaches were shown able to predict similar fluidization behaviors and bubbling phenomena in the context of solids mixing in gas fluidized beds. Slight discrepancies was however found in the solid volume fraction distribution, and severe bed expansions in the initial phases of the process were predicted only by Lagrangian simulations.

The present paper aims at investigating the LMD printing process through both Eulerian-Eulerian (EE) and Lagrangian-Eulerian (LE) approaches, and compare them in terms of computational efficiency, implementation, and physical applicability. To the authors' knowledge there are no publications on this topic in the literature. In particular, performance and accuracy are studied in order to reproduce the shape of the powder cone outside the deposition head, such as its minimum diameter and its positioning, which are the key factors commonly evaluated in the experiments. Thermal properties and heat exchange phenomena of the process are not considered in the present simulations. This is in line with the experimental campaign, our numerical testing refers to, where no laser sources are employed.

Both the EE and LE approaches are implemented in a in-house code using OpenFOAM, a C++ toolbox whose language follows an object-oriented paradigm, allowing to develop customized numerical solvers for the solution of continuum mechanics problems, including CFD [17]. All the numerical outcomes refer to three-dimensional problems.

The paper is organized as follows: in Section 2 the modeling and numerical features for the OpenFOAM implementation are presented and discussed; in Section 3 numerical test are detailed with data concerning the conducted simulation campaign and, eventually, in Section 4 the numerical results are reported and discussed.

2. Problem formulation and implementation

As previously mentioned, different CFD approaches can be adopted to model the physical problem of powder and gas mixture flow during LMD process. From a computational viewpoint, the crucial issue in terms of efficiency and accuracy is the simulation of the particles dynamics [18].

Two approaches can be followed to this purpose, both based on an Eulerian formulation. The former is a pure Eulerian approach, namely the Eulerian-Eulerian (EE) method, where powder and gas are both treated as continuous fluids, and coupled each other with the Navier-Stokes system of equations. The latter is a mixed approach, namely a Lagrangian-Eulerian (LE) method, working with a Lagrangian description of powders as particles that are tracked inside the problem domain, where gas dynamics is simultaneously described as an Eulerian incompressible flow, described by the Navier-Stokes equations. In particular, in the LE approach, the powder diffusion is simulated with a Discrete Parcel Method (DPM) [19], that, instead of solving each individual particle as in the Discrete Element Method (DEM) [20, 21], identifies and tracks a parcel of particles which moves through the flow field. In other words, the parcel is a representative elementary volume of particles, so as to homogenize in a unique macro-particle all powder properties of such a volume (size, velocity, rotational rate, etc.).

2.1. Eulerian-Eulerian (EE) approach

In the Eulerian-Eulerian (EE) approach, the powder-particle phase is treated as an additional continuous phase that interacts with the primary gas-fluid continuous phase. From now on, we indicate with $\boldsymbol{u}$ and $\boldsymbol{g}$ the velocity and gravity vector-fields, respectively, and with p the pressure scalar-field. Introducing an index i to indicate the general phase and assuming $i = \phi$ and $i = \sigma$ for the continuous fluid phase and the particle solid phase, respectively, the governing equations for the Eulerian-Eulerian model are the continuity equations for mass conservation (1a), and the momentum

balances for both continuous phases (1b), *i.e.*:

$$\frac{\partial \epsilon_i}{\partial t} + \nabla \cdot (\epsilon_i \boldsymbol{u}_i) = 0 \tag{1a}$$

$$\rho_i \frac{\partial (\epsilon_i \boldsymbol{u}_i)}{\partial t} + \rho_i \nabla \cdot (\epsilon_i \boldsymbol{u}_i \boldsymbol{u}_i) - \nabla \cdot \epsilon_i \boldsymbol{\tau}_i = -\nabla(\epsilon_i p_i) + \rho_i \epsilon_i \boldsymbol{g} - \boldsymbol{F}_{i,j} \tag{1b}$$

where ϵ_i describes the volumetric fraction of each phase:

$$0 \leq \epsilon_i \leq 1\,, \quad \text{with} \quad \epsilon_\phi + \epsilon_\sigma = 1\,; \tag{2}$$

the phase densities are indicated with ρ_i, while $\boldsymbol{\tau}_i$ is the stress tensor field of each phase:

$$\boldsymbol{\tau}_i = \nu_i \left(\nabla \boldsymbol{u}_i + (\nabla \boldsymbol{u}_i)^T \right) + \left(\lambda_i - \frac{2}{3} \nu_i \right) (\nabla \cdot \boldsymbol{u}_i)\, \boldsymbol{\delta} \tag{3}$$

$\nu_i = \mu_i / \rho_i$ being the i-th phase kinematic viscosity, while μ_i is the corresponding dynamic viscosity, and λ_i is the bulk viscosity, with $\lambda_i = \lambda_\sigma$ if $i = \sigma$ and $\lambda_i = 0$ if $i = \phi$; $\boldsymbol{\delta}$ is the second-order identity tensor.

The term $\boldsymbol{F}_{i,j}$ is the momentum transfer term between the phases i and j; in particular, $\boldsymbol{F}_{\phi,\sigma}$ represents the forces acting on the gas-fluid phase caused by the particle-phase, and conversely, $\boldsymbol{F}_{\sigma,\phi}$ represents the forces acting on the particle-solid phase due to the gas-fluid phase. These forces of momentum transfer are related each other according to the Newton third law:

$$\boldsymbol{F}_{\phi,\sigma} + \boldsymbol{F}_{\sigma,\phi} = 0 \tag{4}$$

Referring to [22], such forces represent just the drag forces contributions, which are usually considered as the most meaningful ones (see also [23]). We then assume:

$$\boldsymbol{F}_{\phi,\sigma} = \beta \left(\boldsymbol{u}_\phi - \boldsymbol{u}_\sigma \right) \tag{5}$$

$$\boldsymbol{F}_{\sigma,\phi} = \beta \left(\boldsymbol{u}_\sigma - \boldsymbol{u}_\phi \right) \tag{6}$$

where β is a momentum exchange coefficient. Several expressions are proposed in the literature to tune such a coefficient. We adopt the drag correlation coefficient proposed

by Gidaspow [24], where the estimated values that Ergun found out for gas volume fractions lower than 0.8, and the ones found out by Wen and Yu for gas volume fractions greater than 0.8, are combined each other (see again [22] for more details). The momentum exchange coefficient turns out to obey to the following expressions:

$$\beta = \begin{cases} 150\dfrac{\epsilon_\sigma^2 \mu_\phi}{\epsilon_\phi d_\sigma^2} + 1.75\epsilon_\sigma \dfrac{\rho_\phi}{d_\sigma}|\boldsymbol{u}_\phi - \boldsymbol{u}_\sigma|, & \epsilon_\phi < 0.8 \\ \dfrac{3}{4} C_D \dfrac{\epsilon_\phi \epsilon_\sigma}{d_\sigma} \rho_\phi |\boldsymbol{u}_\phi - \boldsymbol{u}_\sigma| \epsilon_\phi^{-2.65}, & \epsilon_\phi \geq 0.8 \end{cases} \tag{7}$$

where C_D is the drag coefficient

$$C_D = \begin{cases} \dfrac{24}{Re_\sigma}(1.0 + 0.15\, Re_\sigma^{0.687}), & Re_\sigma \leq 1000 \\ 0.44, & Re_\sigma > 1000 \end{cases}, \tag{8}$$

depending on the particle Reynolds number Re_σ for the solid phase, which is averaged on the cell, and expressed in terms of the average particle diameter d_σ, *i.e.*,

$$Re_\sigma = \frac{\epsilon_\phi \, d_\sigma \, |\boldsymbol{u}_\phi - \boldsymbol{u}_\sigma| \rho_\phi}{\mu_\phi} \, . \tag{9}$$

2.2. Lagrangian-Eulerian (LE) approach

In the Lagrangian-Eulerian (LE) approach, the particle-solid phase is treated through a Lagrangian representation that models and computes the particle evolution. The resulting Lagrangian description is then coupled with the gas-fluid phase, described exactly as in the above mentioned Eulerian model.

The particle evolution is determined on the basis of a particle distribution function $f(\boldsymbol{x}_\sigma, \boldsymbol{u}_\sigma, \rho_\sigma, V_\sigma, t)$, varying on time t and depending on position $\boldsymbol{x}_\sigma$, velocity $\boldsymbol{u}_\sigma$, particle density ρ_σ and volume of the particle V_σ, respectively. From now on, we will adopt the term *parcel*, as the computational entity consisting of N_σ particles – kept constant in time – together with an homogenized set of value $(\boldsymbol{x}_\sigma, \boldsymbol{u}_\sigma, \rho_\sigma, V_\sigma)$.

The distribution function f obeys a phase continuity conditions and, in particular,

satisfies the following transport equation in the phase space:

$$\frac{\partial f}{\partial t} + \nabla \cdot (f\, \boldsymbol{u}_\sigma) + \nabla_v \cdot (f\, \boldsymbol{a}_\sigma) = 0 \tag{10}$$

where ∇_v is the divergence operator respect with to the velocity field, while $\boldsymbol{a}_\sigma$ is the parcel acceleration expressed as:

$$\boldsymbol{a}_\sigma = \beta\left(\boldsymbol{u}_\phi - \boldsymbol{u}_\sigma\right) - \frac{1}{\rho_\sigma}\nabla p + \boldsymbol{g} - \frac{1}{\epsilon_\sigma \rho_\sigma}\nabla \tau_\sigma \tag{11}$$

β being the momentum exchange coefficient already defined in (7), and τ_σ the parcel normal stress. According to Harris and Crighton model [25], τ_σ is obtained on the basis of experimental evidences, and its expression turns out to be:

$$\tau_\sigma = \frac{P_\sigma\, \epsilon_\sigma^\alpha}{\max(\overline{\epsilon}_\sigma - \epsilon_\sigma, \gamma(1 - \epsilon_\sigma))} \tag{12}$$

where P_σ is a constant value of pressure (namely, 100 Pa), α is a dimensionless empirical constant (ranging between 2 and 5), γ is an empirical small number of the order to 10^{-7}, while $\overline{\epsilon}_\sigma$ is a limit value of parcel volume fraction, meaning the maximum value of particles in cubic close-packing mode [25]. The solid volume fraction ϵ_σ is defined by integrating the parcels distribution function as:

$$\epsilon_\sigma = \iiint f\, V_\sigma\, dV_\sigma\, d\rho_\sigma\, d\boldsymbol{u}_\sigma \tag{13}$$

Once the distribution function f is solved by time-integration of (10), the parcels velocity and position are updated in the n-th time step as:

$$\begin{aligned} \boldsymbol{u}_\sigma^{n+1} &= \boldsymbol{u}_\sigma^n + \Delta t\, \boldsymbol{a}_\sigma^n \\ \boldsymbol{x}_\sigma^{n+1} &= \boldsymbol{x}_\sigma^n + \Delta t\, \boldsymbol{u}_\sigma^{n+1} \end{aligned} \tag{14}$$

Note that the collision between the parcels and the wall is taken into consideration for

assuming the following conditions

$$\begin{aligned} \boldsymbol{u}_{\sigma,n}^{n+1} &= -e\,\boldsymbol{u}_{\sigma,n}^{n} \\ \boldsymbol{u}_{\sigma,t}^{n+1} &= (1-f_r)\boldsymbol{u}_{\sigma,t}^{n} \end{aligned} \tag{15}$$

where $\boldsymbol{u}_{\sigma,n}$ and $\boldsymbol{u}_{\sigma,t}$ are the normal and tangential velocities, respectively, and e the coefficient of restitution, whereas f_r the coefficient of kinetic friction. Such coefficients are evaluated on the basis of the specific test to solve, and they will be specified later in the conducted numerical campaign.

Note finally that the momentum transfer term $\boldsymbol{F}_{\sigma,\phi}$ can be obtained from the expression of the parcel acceleration (11), and in line with (13) it can be written as:

$$\boldsymbol{F}_{\sigma,\phi} = \iiint f\, V_\sigma\, \rho_\sigma \left[\beta\left(\boldsymbol{u}_\phi - \boldsymbol{u}_\sigma\right) - \frac{1}{\rho_\sigma}\nabla p\right] dV_\sigma\, d\rho_\sigma\, d\boldsymbol{u}_\sigma \tag{16}$$

2.3. OpenFOAM implementation details

In the Eulerian-Eulerian model, two separate continuous problems for each phase are solved, whence they interact each with other through the interphase transfer equations (4) computing the interphase terms $F_{i,j}$. In the Eulerian-Lagrangian model, the domain of solution is solved only for continuous phase. The parcel path is recovered according to eqs. (10)-(16) within a Lagrangian framework. The Lagrangian simulations are carried out by a particular DPM (Discrete Parcel Method) solver of OpenFOAM, `MPPICFoam` (MultiPhase Particle-In-Cell method [26, 27, 28, 29, 30, 31, 32, 33]), that implements a Lagrangian approach for dense flows. On the other hand, the `twoPhaseEulerFoam` [33] solver is set up to solve the problem with the Eulerian-Eulerian approach. These approaches are described in the OpenFOAM documentation [34].

In this section some numerical details will be provided for the Eulerian computations, while the interested reader can find all the details for the Lagrangian ones in several here mentioned papers, *e.g.*, in [29, 35, 33].

Note that in the Lagrangian-Eulerian approach several quantities computed in Lagrangian form have to be evaluated in Eulerian form. This point is solved by coarse

averaging procedures, that interpolates the Lagrangian properties (i.e., particle volume fraction, particle velocity, and fluid-particle interaction force) from their discrete values to the corresponding Eulerian properties defined on the Eulerian grid. For more details, see [36].

Discretization of the Navier-Stokes equations. Within the Navier-Stokes equations for incompressible flows as adopted in (1), the convection term $\nabla \cdot (\epsilon_i \boldsymbol{u}_i \boldsymbol{u}_i)$ represent the nonlinear contribution to the problem. Several nonlinear solvers can be implemented to handle such a term in the equations but these are in general quite expensive and impractical [37, 38, 39, 40]. Therefore, we linearize the convection term: for a control cell-volume V_σ, with faces f centered around a cell-point P, and all variables defined at the cell center, we use the discretized version of the Gauss theorem to express the discretized version of the convection term as a linear combination of the velocity variables:

$$\int_{V_\sigma} \nabla \cdot (\epsilon_i \boldsymbol{u}_i \boldsymbol{u}_i) dV = \sum_f \Phi \boldsymbol{u}_f \approx a_p \boldsymbol{u}_p + \sum_n a_n \boldsymbol{u}_n \tag{17}$$

All the coefficients a_n and a_p collect the known fluxes $\Phi = \boldsymbol{S} \cdot (\epsilon_i \boldsymbol{u}_i)_f$ across the f-th face of the control volume, and the velocity values at the f-th face are interpolated from the control volume and neighboring volumes by means of the operator $\boldsymbol{S}$, so that $\boldsymbol{u}_p$ represents the velocity for the control cell-volume, $\boldsymbol{u}_n$ the one of neighboring volumes. Note that within this procedure we implicitly assume the phase fraction ϵ_i to be known when computing $\boldsymbol{u}_p$. Moreover, the continuity equation (1a) can be written as:

$$\frac{\partial \epsilon_i}{\partial t} + \sum_f \boldsymbol{S} \cdot (\epsilon_i \boldsymbol{u}_i)_f = 0 \tag{18}$$

when considering some explicit discretization in time.

Derivation of the pressure equation. Once the convection term is linearized, at a given time-step the entire equation (1b) in its discrete form can be represented as follows:

$$\begin{aligned}\left(a'_p - \frac{f_p}{\rho_i}\right)\boldsymbol{u}_p &= -\sum_n a_n \boldsymbol{u}_n + a_0 \boldsymbol{u}_0 + \boldsymbol{g} + \frac{\boldsymbol{F}_{i,j}}{\rho_i} - \nabla p \\ a_p \boldsymbol{u}_p &= \boldsymbol{H}(\boldsymbol{u}_i) - \nabla p \\ \boldsymbol{u}_p &= \frac{\boldsymbol{H}(\boldsymbol{u}_i)}{a_p} - \frac{\nabla p}{a_p}\end{aligned} \tag{19}$$

where all quantities having subscript "$_0$" refer to the known solution at the previous time-step. In the above equation all the diagonal coefficients of the linearized discrete problem are assembled in one coefficient a_p, while $\boldsymbol{H}(\boldsymbol{u}_i)$ collects all off-diagonal contributions of the same linear system, including source terms.

As concerning continuity conditions (1a) and then (18), the velocity of the f-th cell face can be computed as follows:

$$\boldsymbol{u}_f = \left(\frac{\boldsymbol{H}(\boldsymbol{u}_i)}{a_p}\right)_f - \left(\frac{\nabla p}{a_p}\right)_f \tag{20}$$

intending here all quantities interpolated at the f-th face itself. By combining equation (18) with (20) we obtain the pressure equation:

$$\sum_f \boldsymbol{S} \cdot \epsilon_f \left(\frac{\nabla p}{a_p}\right)_f = \frac{\partial \epsilon_i}{\partial t} + \sum_f \boldsymbol{S} \cdot \epsilon_f \left(\frac{\boldsymbol{H}(\boldsymbol{u}_i))}{a_p}\right)_f \tag{21}$$

so that the flux Φ appearing in (17) can be computed as:

$$\Phi = \boldsymbol{S} \cdot (\epsilon_i \boldsymbol{u}_i)_f = \boldsymbol{S} \cdot \epsilon_f \left[\left(\frac{\boldsymbol{H}(\boldsymbol{u}_i))}{a_p}\right)_f - \left(\frac{\nabla p}{a_p}\right)_f\right] \tag{22}$$

`PIMPLE` solver. The solution procedures adopted for both Eulerian and Lagrangian approaches rely on the `PIMPLE` algorithm [41], that merges the PISO [42] algorithm, addressed to recover a pressure correction for the problem, and the SIMPLE [43] algorithm, working as relaxation step of the problem variables. The `PIMPLE` algorithm, that provides at each time-step the velocity vectors $\boldsymbol{u}_i$, proved to have faster convergence than algorithms using such numerical schemes separately (see [41] for more details).

The following steps are iteratively performed in `PIMPLE`:

1. assemble the discretized equation for $\boldsymbol{u}_i$ on the grid without any source terms: a coefficient matrix is set up according to $(19)_1$, source terms not included;
2. relax the equation;
3. solve the equation (19) with a trial value of the pressure field, namely p_0, that corresponds to the pressure field in the previous time-step: such a solution allows us to obtain the momentum predictor $\boldsymbol{u}^\star$ at the cell centers;
4. using the predictor $\boldsymbol{u}^\star$, assemble the operator $\boldsymbol{H}(\boldsymbol{u}^\star)$ and interpolate both a_p and $\boldsymbol{H}(\boldsymbol{u}^\star)$ to the cell faces;
5. solve the pressure equation (21) at the cell faces;
6. update by (22) the flux field at the cell faces;
7. relax the pressure;
8. update by (19) the velocity at the cell centres;
9. update the boundary conditions for consistency.

3. Numerical campaign targeted to experimental investigation

In this Section we provide several settings of the numerical campaign, addressed also to have a preliminary comparison between numerical simulations and experimental evidences. In particular, we refer to the pilot experimental study conducted by PoliMi [44], where the Additube LMD system (BLM Group), using a triaxial nozzle has been employed (see Figure 1). In the same Figure a schematic view of the LMD process is shown, and the reader can refer to [2] for more details.

Geometry and physical settings. The tested geometry of the LMD printer consists of a nozzle with an height of 42 mm, the powder channels inclined by 21^o, with a diameter of 2.5 mm, and the laser channel with diameter of 6 mm (see Figure 2).

Since we are dealing with a metallic powder, we describe it with the following assumptions: i) the particles are considered to be spherical; ii) all the particles have the same radius, *i.e.*, the mean radius of a normal distribution; iii) the size of the particles does not change in time. The density of the particles is larger that the gas density

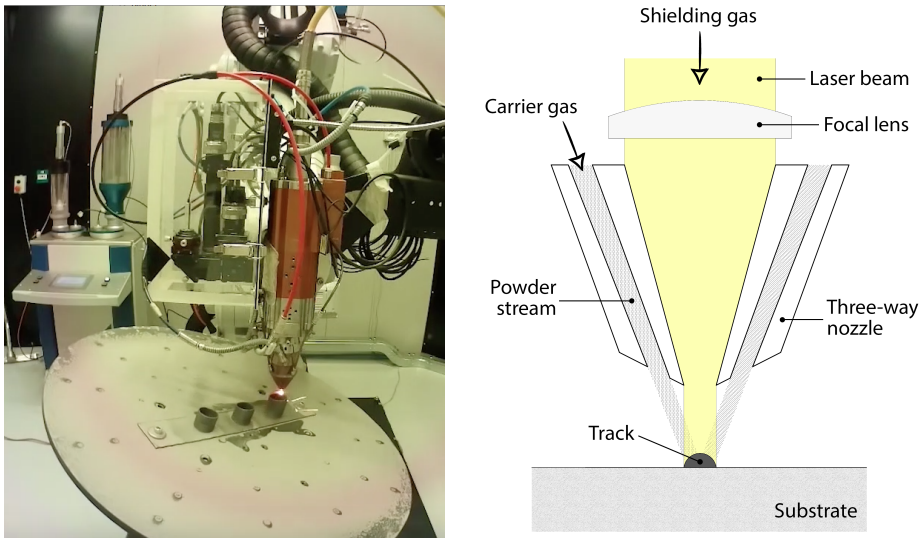

Figure 1: Laser Metal Deposition machine built by Politecnico di Milano on the left; a sketch of the process on the right.

($\rho_\sigma \gg \rho_\phi$) and we assume the gas density ρ_ϕ to be equal to 1.145 kg/m^3, and the metal powder density ρ_σ to be equal to 8000 kg/m^3. This allows to consider the drag force as the main cause of the particle motion. Moreover, the nitrogen kinematic viscosity ν_ϕ is set equal to $15 \cdot 10^{-6}$ m^2/s, whereas, since in the Eulerian-Eulerian approach we describe metal powder as an equivalent fluid, we compute the kinematic viscosity associated to the solid phase, ν_σ, using the kinetic theory of granular flow implemented in OpenFOAM [45].

Velocities inlets of both gas and particles are directly taken from the experiments and are used as boundary conditions of the problem. In the experiments (see Sec. 4.4) particle velocities proved to be strongly affected by nitrogen flow rate inserted in the system, specifically set to the values $\{5, 7.5, 10\}\, l/min$. Hence, we impose inlet velocities equal to $\{1.4, 1.6, 1.8\}\, m/s$, for both particles and gas phases, disregarding to accurately reproduce the flow developing along the nozzle channels.

The values of powder and gas flow rate allowed us to identify the number of particles and the particle volume fraction to impose at the inlet boundaries. In particular the fluid-particle regime is a collision-dominated dense flow, with volume fractions ranging between 0.001 and 0.1 (see [19] for more details).

The Reynolds number is estimated under the hypothesis of a fluid velocity equivalent to the maximum value imposed at the inlet, that is 1.8 m/s. The resulting Reynolds number, about 300, is consistent with the assumption of a flow modeled in laminar regime. Moreover, the particle size ensures that fluid-solid interaction does not cause turbulence phenomena, as showed by Kussin and Sommerfeld in [46], where the turbulence intensity decreases significantly for particles with diameter ranging between 60 μm and 190 μm.

For the gas phase, no-slip conditions are considered along the nozzle head channel walls; for the particle phase, in the Eulerian formulation slip condition at the walls are assumed, whereas, in the Lagrangian framework the non-dimensional coefficients of restitution and kinetic friction are set equal to $e = 0.97$ and $f_r = 0.09$, respectively, to model the particle collision with the walls as expressed in eq. (15). Such coefficients are determined by considering spherical steel particles which exhibit a low loss of kinetic energy when impacting with walls [47].

As concerning the boundary conditions imposed for the Navier-Stokes problem, the pressure at the outlet is imposed to be to equal to the atmospheric pressure, while at the inlet the velocity is fixed to the values described above. For more details regarding how OpenFOAM numerically handles such a type of Navier-Stokes boundary conditions see [34].

Discretization and numerical settings. The computational domain consists of a cylinder in which the nozzle is included, thus defining the whole computational domain as depicted in Figure 2.

The deposition head is formed by three channels, in which gas and particles pass through, and an additional channel, bigger than others and positioned at the center of the nozzle, accounted for laser beam irradiation. The domain is discretized using tetrahedral elements. The mesh has to be fine enough to reach small Courant number and make the simulation stable, but a severe limitation of the solver occurs in the case of the Eulerian-Lagrangian approach. In fact, the size of the particles must be sufficiently small in comparison with the computational grid so as to allow the coarse averaging procedures (see Sec. 2.3) to provide accurate interpolations of the Lagrangian proper-

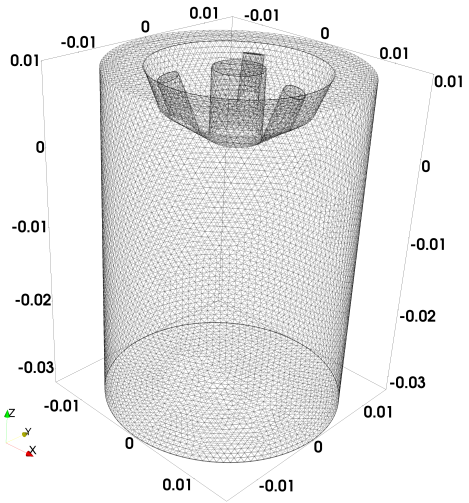

Figure 2: Computational domain used for both Eulerian-Eulerian and Lagrangian-Eulerian approaches

ties, i.e., particle volume fraction, particle velocity, and fluid-particle interaction force [36].

The smallness of the Courant number influences also the time-step size which is set to $1 \cdot 10^{-5}$ s in our computations. The time discretization methods of explicit Euler scheme and Runge-Kutta scheme are employed for solving in time the Navier-Stokes momentum equation (1b) and the transport equation (10), respectively. As concerns the spatial discretization, we adopted a standard finite volume approach using Gaussian integration with linear interpolation (central difference method), so as to compute gradient, laplacian, and divergence operators. See [34] for more details.

4. Numerical results

In order compare the Eulerian-Eulerian (EE) and the Lagrangian-Eulerian (LE) approaches, we first performed a preliminary investigation at the inlet to have the two models to be comparable from a physical viewpoint. Then, volume fraction and velocity fields are carefully compared in terms of both gas and solid phases.

The numerical campaign is also driven in order to determine the properties of the powder cone, specifically: (i) the minimum diameter of powder cone [mm]; (ii) the

distance of the minimum diameter from the exit of the nozzle [mm]; (iii) the particle velocity [m/s]. Such properties defining the powder shape cone outside the deposition head are conceived as testbeds for future works of identification and validation with experiments. A preliminary, qualitative, comparison is introduced at the end of the present Section, to show the capability of the developed numerical schemes on predicting experimented trends.

4.1. On the comparability of the two approaches

The goal of the first test is to compare the amount of solid fraction, i.e., the mass, entering in the domain for both the approaches. For the Eulerian-Eulerian approach the solid volume fraction is directly imposed, whereas, for the Eulerian-Lagrangian approach, the number of particles has to be assigned at the boundary inlets. These two different input data, that represent the same mass, must return the same conditions at the inlet.

Within the EL approach, the number of particles to impose at the inlet of a single channel is estimated as follows. Let be V_ϕ the known volume of a single particle and ρ_ϕ its relative density. Then, the mass of a particle, m_ϕ can be simply calculated as the product between V_ϕ and ρ_ϕ. Known the mass m_ϕ, the number of particles per second to be introduced in each single channel can be evaluated as:

$$n_\phi = \frac{Q_\phi}{m_\phi} \frac{T_{sim}}{n_{ch}} \tag{23}$$

where Q_ϕ is the total powder flow rate, n_{ch} the number of nozzle channels and T_{sim} the simulation time.

Regarding the EE approach, the mass relative to the particles to introduce in the system, as boundary condition at the inlet, has to be computed in terms of solid volume fraction, which is defined as:

$$\alpha_p = \frac{\sum_i V_{\phi,i}}{V_{tot}} \tag{24}$$

where $V_{tot} = \sum_i V_{\phi,i} + V_\sigma$ is the total volume introduced in the system, defined as the sum of the particles volume plus the carrier gas volume. The volume occupied by the particles $\sum_i V_{\phi,i}$ is directly derived from eq. (23) as the product between the volume

of a sigle particle V_ϕ and the number of particles introduced at the inlet n_ϕ. On the other hand, the volume occupied by the gas phase is evaluated assuming a uniform velocity field of the gas phase $\boldsymbol{u}_\sigma$ at the inlet. Then the carrier gas volume injected through the channels is obtained as:

$$V_\sigma = \boldsymbol{u}_\sigma \sum_i A_{ch,i}\, T_{sim} \tag{25}$$

where $\sum_i A_{ch,i}$ is the sum of all channels area. This procedure is expected to ensure the same boundary conditions for both simulations.

Figure 3 depicts a color map of the volume fraction distributions at the inlet of the nozzle channels, for both the approaches. Such a figure proves that the inlet amount of density of the solid fraction entering in the domain is definitely equal for both the approaches, except for a small difference due to the speckled behaviour of the EL approach. Such a behaviour is due to the non-uniformity of the particle distribution in the computational domain, that is characterized by a random positioning at the inlet, and governed by a flow rate according with boundary conditions.

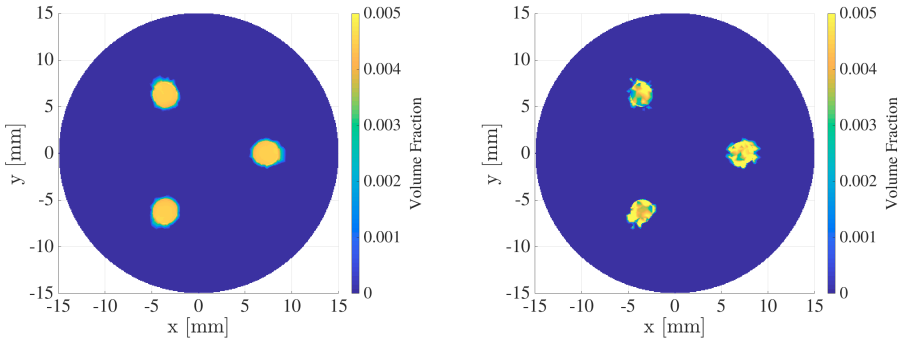

Figure 3: Color maps representing volume fraction distribution at the inlet. Eulerian-Eulerian approach (on the left) and Eulerian-Lagrangian approach (on the right). In the Lagrangian-Eulerian case, the volume fraction representation in non uniform due to the presence of solid particles.

The comparability of the two approaches is finally validated by considering the mass distribution at regime. As specified in the conservation equations, the mass is expected to be preserved. In Figure 4 we then report the flow of the volume fraction, for both the solid and the gas phases, either inside and outside the nozzle, where the deposition process occurs. Note that the volume fraction flow is obtained by numerically

integrating the pointwise values of the volume fraction. Such values are given for each cell of the computational domain (see Figure 2): then, fixing a certain value of z, for all the cells in the range $[z - \epsilon, z + \epsilon]$, with $\epsilon = 1\,mm$, we integrate through the midpoint rule the discrete volume fraction distribution to evaluate its flow value associated with z.

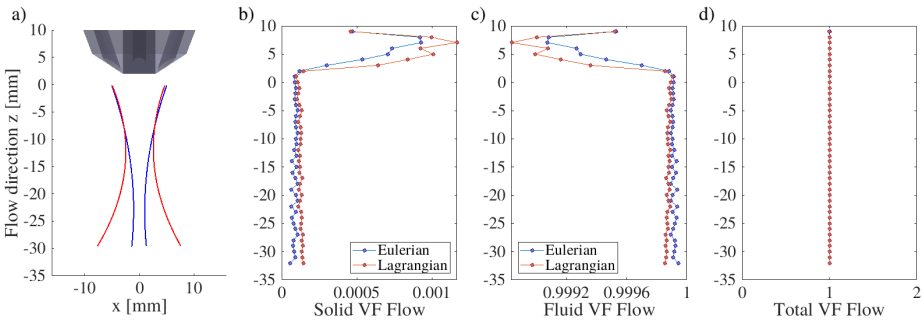

Figure 4: Comparison between Eulerian-Eulerian simulation (blue lines) and Lagrangian-Eulerian's (red lines). Figure a) reports the outline of the nozzle and the powder cone shape. Figures b) and c) show the solid and fluid volume fraction (VF) flow rate along the z-direction, respectively. The total volume fraction flow rate, that is the sum of the two previous quantities, is depicted in Figure d).

Figure 4(a) represents the powder outline formed below the nozzle. As explained in Section 1, such a result emphasizes the main difference between the two approaches. With the Eulerian-Lagrangian approach, the powder ejected from the nozzle forms ah hourglass-like shape, whereas the powder outline obtained with the Eulerian-Eulerian approach remains constant after convergence of the powder streams. This behavior is due to the fact that Eulerian-Eulerian methods do not represent more than one velocity value for each phase in one computational cell, and then it can not capture crossing trajectories. This point will be further investigated later. As expected, the total mass is preserved and there are no appreciable differences between the approaches (Figure 4(d)). Figure 4(b-c) prove that the volume fraction distributions obtained with the two different approaches are very similar, for both solid and gas phases. The two simulations slightly differ in the upper zones inside the nozzle, where the flows of volume fraction of both phases grow up as densities increase in the channels.

4.2. Velocity and mass fields

In this Section a comparison between the two approaches in terms of velocity and mass flows fields, measured in different ways, is reported. Figures 5 and 6 depict the velocity-magnitude 3D fields associated with the two phases respectively. For the solid phase (see Figures 5), the velocity fields of the two approaches appear quite similar in terms of magnitude. However, as mentioned in the previous section, the approaches significantly differ: the EE approach cannot reproduce the crossing trajectories predicted by the EL approach, which directly represents the velocity of each particle.

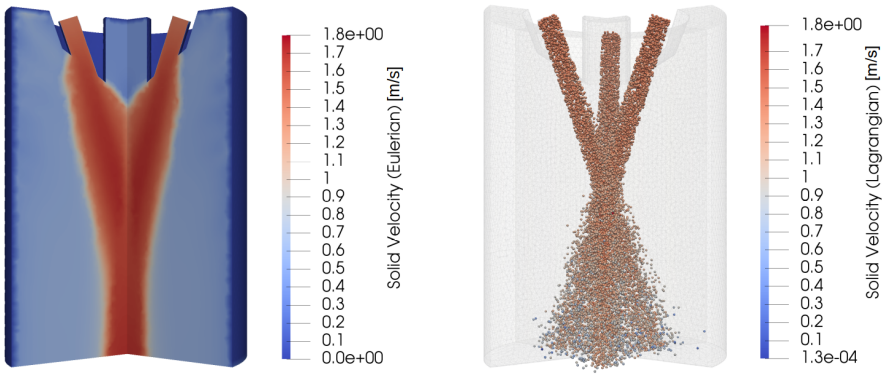

Figure 5: Magnitude of particles velocity field. Eulerian-Eulerian approach (on the left) and Lagrangian-Eulerian approach (on the right).

On the other hand, for the gas phase, the magnitude of the velocity field estimated by the EE approach differs from the one predicted by the LE approach (see Figures 6).

Such a result is furthermore emphasized by Figure 7, where the mass flow rates are reported along the z-direction (flow quantities are computed as done for Figure 4). Figure 7(b-c) confirm the results obtained in Figures 5 and 6: except for the part inside the nozzle, the solid mass flow rate calculated with the EL approach is slightly higher than the same quantity computed by the EE (Figure 7(b)), while the EE approach overestimates the mass flow rate associated with the gas phase (Figure 7(c)).
As concerning the solid phase, although small, the gap of mass flow rates between the two approaches is due to the different way of computing velocities: in the EE approach

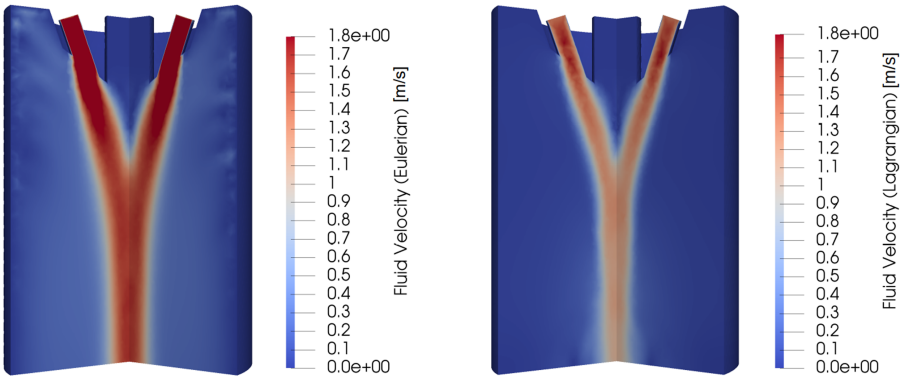

Figure 6: Magnitude of gas velocity field. Eulerian-Eulerian approach (on the left) and Lagrangian-Eulerian approach (on the right).

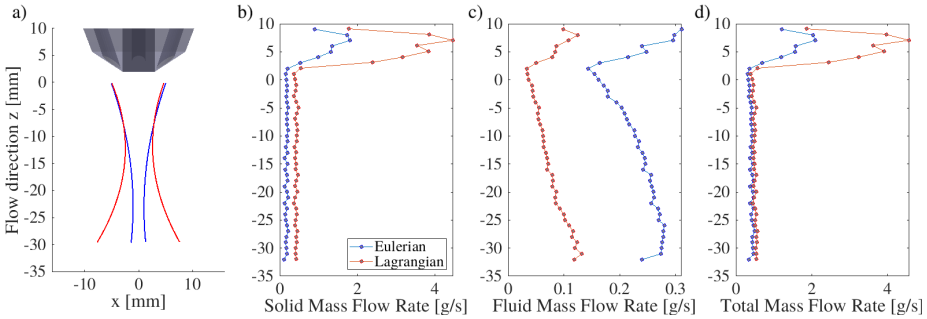

Figure 7: Mass flow rates along the z-direction. Comparison between Eulerian-Eulerian (blue) and Lagrangian-Eulerian (red) approach.

the velocity of the particles represents an average value calculated in each computational cell (see Figure 7(b)) and this can lead to an underestimation of the actual velocity of each particle, which on the contrary are explicitly computed in the LE approach as pointwise value, in the spirit of the Lagrangian description.

The evaluation of the mass flow rate associated with the gas phase shows an opposite trend (see Figure 7(c)). Such a rate computed by the EL approach is lower than that predicted in the EE approach. This result can be seen as a consequence of the momentum balance (see eq. (1b)), that is numerically confirmed by Figure 7(d) showing how the total amount of mass flow rate is predicted very similarly in both the approaches.

Note that all such comments are valid only for the behavior outside the deposition head,

whereas inside the nozzle channels discrepancies between the two approaches are evident. Especially in the evaluation of the solid phase, and in agreement with the results depicted in Figure 4, a relevant increase of the mass flow rate is predicted by the EL approach in contrast with the EE approach. In fact, inside the nozzle channels the solid mass is greater than the fluid mass (see again Figure 4(b-c)): while the solid volume fraction reaches inside the channels a maximum value which is about 8 times the value outside the channels, the values of the gas volume fraction vary less than 1%.

The results regarding the velocity and mass field obtained with the two approaches are finally summarized in terms of mass flow ratio, mass ratio, and velocity ratio, respectively (see Figures 8). All such quantities are computed for a given time at each cross section. The mass flow ratio is computed as the ratio between the mass flow rate

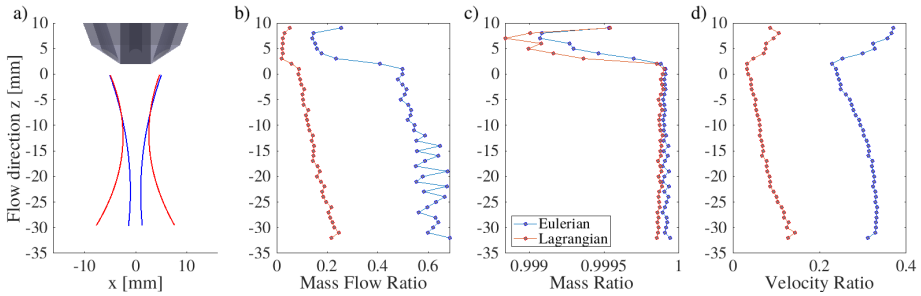

Figure 8: Mass flow ratio, mass ratio, and velocity ratio along the z-direction. Comparison between Eulerian-Eulerian (blue) and Lagrangian-Eulerian (red) approach.

of the fluid phase and the total mass flow rate; the mass ratio is computed as the ratio between the fluid volume fraction and the total volume fraction; the velocity ratio is computed as the ratio between z-direction velocity component of the fluid phase and the one of the solid phase.

The different predictions of the two approaches discussed above are here emphasized by the fact that both mass flow and velocity ratios are overestimated by the EE approach with respect to the EL approach, although the estimations of the mass ratio are very close in the two approaches.

4.3. Powder shape cone

In this Section, we report the predictions offered by the two approaches for what concerns the most significant quantities from an engineering viewpoint, i.e., the powder stream structure formed by the triaxial nozzle and its cone shape. More specifically, such quantities allow us to estimate the minimum diameter size below the nozzle, as we will present in the next Section.

Figure 9 shows the powder flux simulated by the EE approach in terms of volume fraction distribution. On the left a 3D representation of the ejection process is depicted, with a color scale mapping the values of particles volume fraction (red color corresponding to high values). On the right, the volume fraction distributions are represented on a X-Z plane cutting the central axis of the domain, that is where maximum particles concentration is reached. This figure shows that, as expected, the highest amount of volume fraction rise at the focal point, *i.e.* where fluxes cross each other.

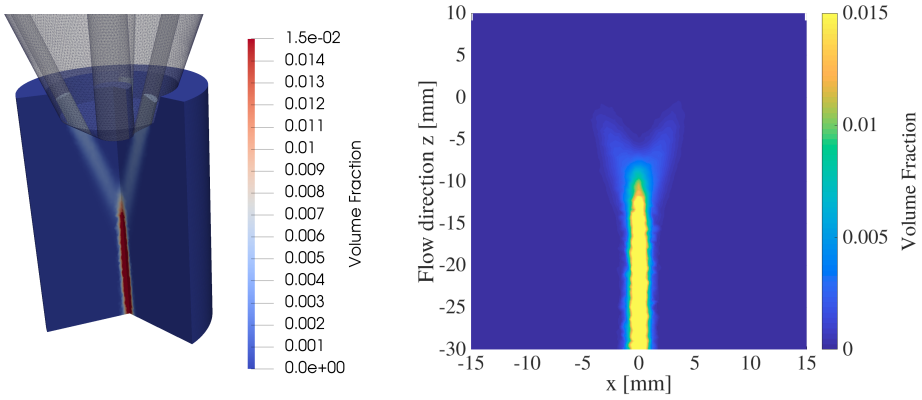

Figure 9: Eulerian 3D Simulation via Eulerian-Eulerian approach: screenshot of the simulation (on the left), particle volume fraction (on the right).

The EL simulations are reported in Figure 10, where the same representations as above are depicted. In this approach, in contrast with the EE approach, the volume fraction of the solid phase is post-processed by using the information regarding the volume fraction of the fluid phase, which is computed in the Eulerian mesh: in each cell of the mesh, we then compute the particles volume fraction as $\epsilon_\sigma = 1 - \epsilon_\phi$.

Figure 11 reports a comparison between the Eulerian-Eulerian and the Lagrangian-Eulerian simulations in terms of powder cone shape. In particular, these trends are

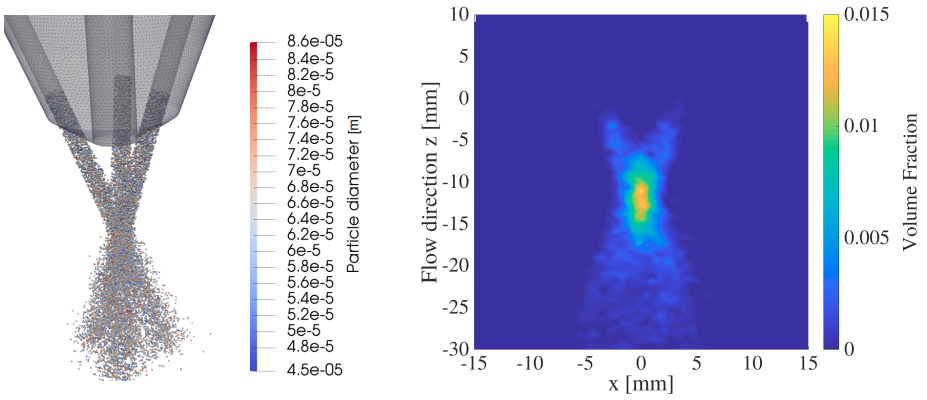

Figure 10: Lagrangian 3D Simulation via Lagrangian-Eulerian approach: screenshot of the simulation (on the left), particle volume fraction (on the right).

determined using a 3rd-order polynomial function that interpolates the most external particles, starting from the central axis, in order to capture the shape of the power flux.

As already mentioned, Figure 11 shows the key difference between the two approaches: the Eulerian-Eulerian method (blue line on the left) can not capture crossing trajectories and the three powder fluxes exiting from the nozzle merge each other in a single stream. Such a result is a consequence of the different formulations employed for the numerical approaches. In the Eulerian formulation the kinematics of the solid phase is represented only in terms of nodal values in the Finite Element mesh, while in the Lagrangian formulation the solid phase consist of particle-points that can move independently in the domain. When the flows of the three solid phases cross each other at a certain point of the domain (the focal point), the resulting velocity in the nodes is averaged in the Eulerian approach (see again Figure 6), thus configuring a single flow of increased density (see again Figure 9). On the contrary, the Lagrangian-Eulerian method (red line on the right of the same Figure) can reproduce the experimented behavior, that is the enlargement of total flux after particles have crossed each other in the focal point (see again Figure 10).

Finally, the two approaches are compared in terms of CPU times. All tests are conducted on an off-the-shelf desktop computer with eight-cores Intel Core i7-6700 running at 3.40 GHz, with 24 GB of RAM, on 64-bit Ubuntu Linux 18.04.4 LTS. Note that the computational time of the Eulerian-Eulerian approach is independent from the

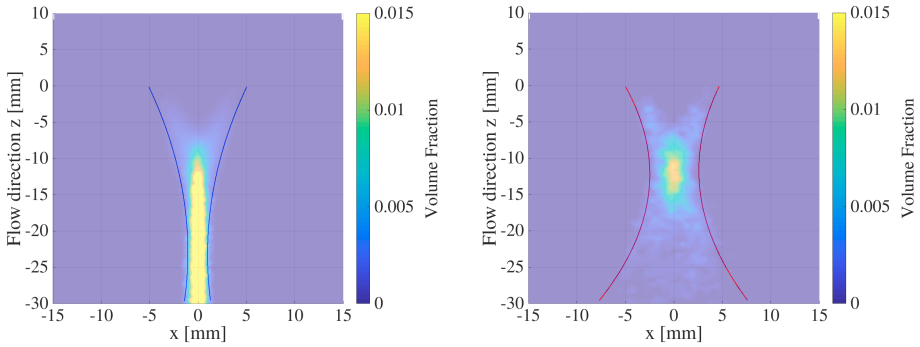

Figure 11: Comparison between Eulerian-Eulerian (on the left) and Lagrangian-Eulerian (on the right) simulations in terms of volume fraction and powder cone shape.

mass flow rate considered at the inlet, whereas the Lagrangian-Eulerian one increases as the number of particles introduced in the process grows. In particular, as depicted in Figure 12, the LE approach has better performances than the EE approach when the number of particles is less than 10^5. For values greater than 10^5, the former tends to become more and more slow than the latter, costing up to six times more in the case of 10^6 particles.

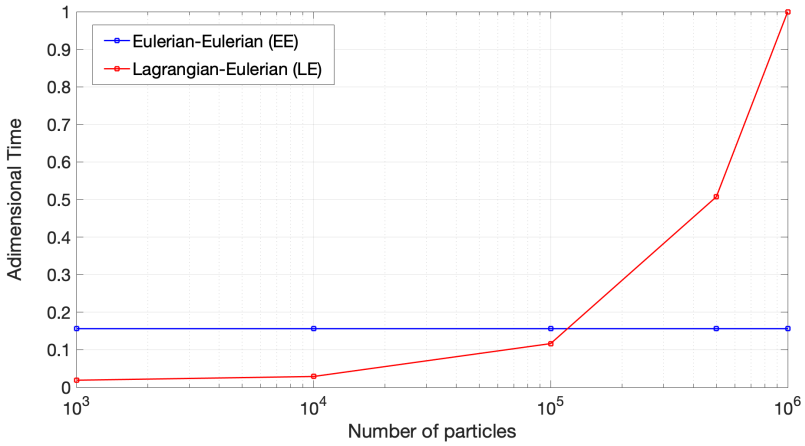

Figure 12: Comparison between Eulerian-Eulerian approach and Lagrangian-Eulerian approach in terms of CPU times nondimensionalized with respect to the maximum value 5540 secs. of CPU time required by LE running with 10^6 particles.

4.4. Towards experimental validation

We present here a preliminary comparison with the outcomes of an experimental campaign conducted by PoliMi. In the employed LMD machine the powder is delivered throughout a powder feeder (GTV Twin PF 2/2-MF) used to manage the powder flow rate. The powder is stored in a hopper and it is gradually spread on a disc able to rotate. The powder flows are directed in the three-way nozzle by means of a powder splitter, which splits the carrier gas in three equal flows. The three-way nozzle is also connected to a laser head (KUKA REIS MWO-I), mounted on a 6-axis anthropomorphic robot (ABB IRB 4600-45), and equipped with a 200 mm focal lens and a 129 mm collimation lens with variable position. The experimental campaign is performed only on the factors affecting the powder cone without laser beam interaction.

By varying the amount of powder, as well as the carrier and shielding gas flow rate, several configurations of particle cone shape and particle velocity can occur. Side-view images of the powder flow shape formed outside the working nozzle are carried out for these purposes. Pictures are captured with a high speed camera converted into binary format and then post-processed by means of the MATLAB Image Processing Toolbox. For each 2D picture, such a toolbox stores the first white pixel on every row of pixels, starting from left and right sides at the same time. This procedure provides an outline of the cone shape. On the other hand, the measurement of the powder velocity is performed tracking the particles distribution exiting from the nozzle. Thanks to a binarization image process, the maximum pixel distance of a particle trace can be obtained, to calculate the local particle velocities. An example of a binarizated picture used to compute the LMD flow features is shown in Figure 13.

The results of experimental data produced by PoliMi are then compared with Eulerian-Lagrangian numerical simulations. Figure 14 shows that simulations are able to capture the trend of the minimum diameter, changing the carrier gas flow rate, but not the absolute values of minimum diameter. This aspect is mainly due to the uncertainty regarding the geometric dimensions of the nozzle that significantly affects the results of the ejection process. In fact, the inclination and the dimensions of the channels, where both powder and carrier gas stream out, are not known a priori and they can only be estimated with appropriate measurements, not provided by the manufacturer.

Figure 13: Images displaying the binarization process. The image on the left is the original frame withdrawn from the imaging experiment. The one on the right shows the binary image after post-processing

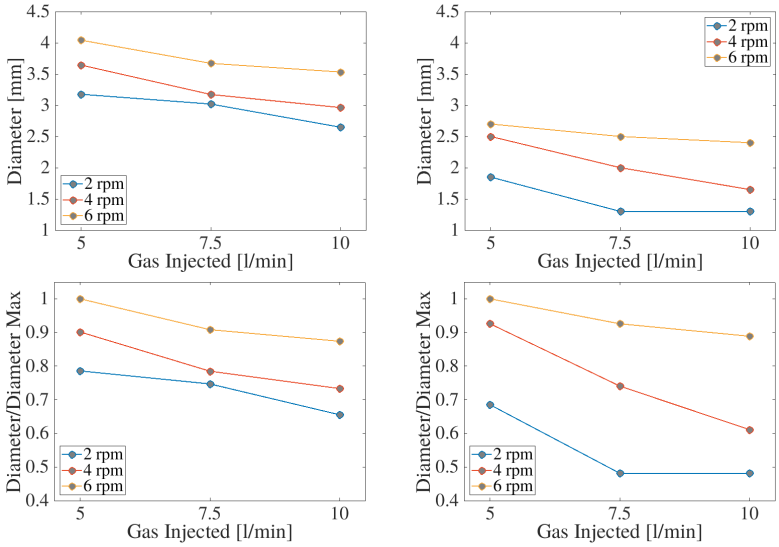

Figure 14: Comparison between our simulations (on the left) and PoliMi experimental data (on the right), in terms of both dimensional (on the top) and nondimensional diameter (on the bottom).

5. Concluding remarks

The present paper proposed a numerical investigation of the LMD printing process by comparing two different approaches, namely an Eulerian-Eulerian (EE) and a Lagrangian-Eulerian (LE). The ensuing strategies were developed and implemented in a in-house code customizing OpenFOAM libraries and tools.

The numerical campaign, all referred to a three-dimensional problem, was addressed to highlight performance of the two approaches, measuring the geometrical key features of the powder shape cone, outside the deposition head. Among the obtained results, the EE method proved to be not able to capture crossing trajectories, carrying out a merged powder flux exiting from the nozzle as a single high-density stream. On the contrary, the LE method was able to predict the experimented behavior, where the total flux divaricates in three streams after particles cross each other in the focal point. However, the EE approach, as well as LE's, reproduced the solid volume fraction amount around the focal point, which is definitely one of the key information in the set up of the LMD printing process.

Additionally, the efficiency of the two approaches was investigated in terms of CPU times, showing that the LE simulation turns out to be more expensive than EE's, as the number of simulated particles increases.

Finally, a preliminary validation with some experiments conducted by PoliMi was reported. Note that in such experiments no laser sources are employed, and as consequence no thermal effects were considered in our work. Although in a qualitative sense, the developed numerical schemes was definitely capable to predict measured decreasing trends of the cone diameter for increasing injected gas velocities.

Acknowledgements

This work was partially supported by the Regione Lombardia through the project "MADE4LO – Metal ADditivE for LOmbardy" (No. 240963) within the POR FESR 2014-2020 program.

References

[1] Q. Zeng, Z. Xu, Y. Tian, Y. Qin, Advancement in additive manufacturing & numerical modelling considerations of direct energy deposition process, in: Y. M. Goy, K. Case (Eds.), Proceeding of the 14th International Conference on Manufacturing Research, ICMR, IOS Press, Amsterdam, 2016, pp. 104–109.

[2] B. S. I. Gibson, D.W. Rosen, Additive Manufacturing Technologies, Springer, 2010.

[3] J. Arrizubieta, J. Ruiz, S. Martinez, E. Ukar, A. Lamikiz, Intelligent nozzle design for the Laser Metal Deposition process in the Industry 4.0, Procedia Manufacturing 13 (2017) 1237–1244.

[4] F. Brueckner, M. Riede, M. Müller, F. Marquardt, R. Willner, A. Seidel, E. Lopéz, C. Leyens, E. Beyer, Enhanced manufacturing possibilities using multi-materials in laser metal deposition, Journal of Laser Applications (2018).

[5] T. Yamada, S. Hasegawa, Y. Kinoshita, S. Yamada, M. Inoue, C. Rosebrock, S. Bracke, Process integration concept for waste reduction among manufacturing planning, modularization and validation, Procedia Manufacturing 21 (2018) 337–344.

[6] H. Pan, F. Liou, Numerical simulation of metallic powder flow in a coaxial nozzle for the laser aided deposition process, Journal of Materials Processing Technology 168 (2) (2005) 230–244.

[7] Y. D. T. Heng Pan, Todd Sparks, F. Liou, The Investigation of Gravity-Driven Metal Powder Flow in Coaxial Nozzle for Laser-Aided Direct Metal Deposition Process, Journal of Manufacturing Science and Engineering 128 (2006) 541–553.

[8] B. Zhang, C. Coddet, Numerical study on the effect of pressure and nozzle dimension on particle distribution and velocity in laser cladding under vacuum base on CFD, Journal of Manufacturing Processes 23 (2016) 54–60.

[9] I. Tabernero, A. Lamikiz, E. Ukar, L. L. de Lacalle, C. Angulo, G. Urbikain, Numerical simulation and experimental validation of powder flux distribution in coaxial laser cladding, Journal of Materials Processing Technology 210 (15) (2010) 2125–2134.

[10] J. Arrizubieta, I. Tabernero, J. E. Ruiz, A. Lamikiz, S. Martinez, E. Ukar, Continuous Coaxial Nozzle Design for LMD based on Numerical Simulation, Physics Procedia 56 (2014) 429–438.

[11] P. Balu, P. Leggett, R. Kovacevic, Parametric study on a coaxial multi-material powder flow in laser-based powder deposition process, Journal of Materials Processing Technology 212 (7) (2012) 1598–1610.

[12] A. Grigoryants, R. Tretyakov, I. Shiganov, A. Stavertiy, Optimization of the shape of nozzles for coaxial laser cladding, Welding International 29 (8) (2015) 639–642.

[13] R. K. S. Liu, Y. Zhang, Numerical Simulation and Experimental Study of Powder Flow Distribution in High Power Direct Diode Laser Cladding Process, Lasers in Manufacturing and Materials Processing 2 (4) (2015) 199–218.

[14] J. J. Nijdam, B. Guo, D. F. Fletcher, T. A. Langrish, Lagrangian and Eulerian models for simulating turbulent dispersion and coalescence of droplets within a spray, Applied Mathematical Modelling 30 (2006) 1196–1211.

[15] R. Z. A. Vié, H. Pouransari, A. Mani, Comparison between lagrangian and eulerian methods for the simulation of particle-laden flows subject to radiative heating, Center for Turbulence Research. Annual Research Briefs 2014 (2014).

[16] J. L. Lee, E. W. C. Lim, Comparisons of Eulerian-Eulerian and CFD-DEM simulations of mixing behaviors in bubbling fluidized beds, Powder Technology 318 (2017) 193–205.

[17] H. Jasak, Openfoam: open source cfd in research and industry, International Journal of Naval Architecture and Ocean Engineering 1 (2) (2009) 89–94.

[18] K. Cheng, Y. Wang, Q. Yang, A semi-resolved CFD-DEM model for seepage-induced fine particle migration in gap-graded soils, Computers and Geotechnics 100 (2018) 30–51.

[19] C. Crowe, J. Schwarzkopf, M. Sommerfeld, Y. Tsuji, Multiphase Flows with Droplets and Particles, Taylor & Francis, 1997.

[20] S. Schmelzle, E. Asylbekov, B. Radel, H. Nirschl, Modelling of partially wet particles in DEM simulations of a solid mixing process, Powder Technology 338 (2018) 354–364.

[21] V. Vivacqua, A. López, R. Hammond, M. Ghadiri, DEM analysis of the effect of particle shape, cohesion and strain rate on powder rheometry, Powder Technology 342 (2019) 653–663.

[22] D. Hirche, F. Birkholz, O. Hinrichsen, A hybrid eulerian-eulerian-lagrangian model for gas-solid simulations, Chemical Engineering Journal 377 (2019) 119743.

[23] Y. Wang, L. Zhou, Q. Yang, Hydro-mechanical analysis of calcareous sand with a new shape-dependent fluid-particle drag model integrated into CFD-DEM coupling program, Powder Technology 344 (2019) 108–120.

[24] D. Gidaspow, Multiphase flow and fluidization: continuum and kinetic theory descriptions, Academic press, 1994.

[25] S. Harris, D. Crighton, Solitons, solitary waves, and voidage disturbances in gas-fluidized beds, Journal of Fluid Mechanics 266 (1994) 243–276.

[26] M. Andrews, P. O'Rourke, The multiphase particle-in-cell (MP-PIC) method for dense particulate flows, International Journal of Multiphase Flow 22 (2) (1996) 379–402.

[27] M. Feng, F. Li, W. Wang, J. Li, Parametric study for MP-PIC simulation of bubbling fluidized beds with Geldart A particles, Powder Technology 328 (2018) 215–226.

[28] S. Yang, H. Wu, W. Lin, H. Li, Q. Zhu, An exploratory study of three-dimensional MP-PIC-based simulation of bubbling fluidized beds with and without baffles, Particuology 39 (2018) 68–77.

[29] F. Li, F. Song, S. Benyahia, W. Wang, J. Li, MP-PIC simulation of CFB riser with EMMS-based drag model, Chemical Engineering Science 82 (2012) 104–113.

[30] H. Razmi, A. S. Goharrizi, A. Mohebbi, CFD simulation of an industrial hydrocyclone based on multiphase particle in cell (MPPIC) method, Separation and Purification Technology 209 (2019) 851–862.

[31] Q. Ma, F. Lei, X. Xu, Y. Xiao, Three-dimensional full-loop simulation of a high-density CFB with standpipe aeration experiments, Powder Technology 320 (2017) 574–585.

[32] S. Karimipour, T. Pugsley, Application of the particle in cell approach for the simulation of bubbling fluidized beds of Geldart A particles, Powder Technology 220 (2012) 63–69.

[33] A. Stroh, F. Alobaid, M. T. Hasenzahl, J. Hilz, J. Ströhle, B. Epple, Comparison of three different CFD methods for dense fluidized beds and validation by a cold flow experiment, Particuology 29 (2016) 34–47.

[34] C. J. Greenshields, OpenFOAM User Guide - Version 5.0 (2017).

[35] K. Luo, F. Wu, S. Yang, J. Fan, CFD-DEM study of mixing and dispersion behaviors of solid phase in a bubbling fluidized bed, Powder Technology 274 (2015) 482–493.

[36] D. Fantin, Towards Fluid-Particle Simulation. CFD-DEM Coupling, Ph.D. thesis, Delft University of Technology (2018).

[37] P. Minev, P. N. Vabishchevich, Splitting schemes for the stress formulation of the incompressible Navier-Stokes equations, Journal of Computational and Applied Mathematics 344 (2018) 807–818.

[38] J. Guermond, P. Minev, A new class of massively parallel direction splitting for the incompressible Navier–Stokes equations, Computer Methods in Applied Mechanics and Engineering 200 (23) (2011) 2083–2093.

[39] P. Birken, A. Jameson, Nonlinear iterative solvers for unsteady Navier-Stokes equations, Proceedings of Symposia in Applied Mathematics (2009) 429–437.

[40] S. S. Clift, P. A. Forsyth, Linear and non-linear iterative methods for the incompressible Navier-Stokes equations, International Journal for Numerical Methods in Fluids 18 (3) (1994) 229–256.

[41] A. Passalacqua, R. Fox, Implementation of an iterative solution procedure for multi-fluid gas-particle flow models on unstructured grids, Powder Technology 213 (1) (2011) 174–187.

[42] C. M. Venier, C. I. Pairetti, S. M. Damian, N. M. Nigro, On the stability analysis of the PISO algorithm on collocated grids, Computers & Fluids 147 (2017) 25–40.

[43] H. Xiao, J. Wang, Z. Liu, W. Liu, A consistent SIMPLE algorithm with extra explicit prediction — SIMPLEPC, International Journal of Heat and Mass Transfer 120 (2018) 1255–1265.

[44] I. Erhardt, Investigation of the powder cone in laser metal deposition, Master of Science in Engineering Management, Department of Management, Economics and Industrial Engineering, Politecnico di Milano (2017).

[45] T. Engen, Cfd analysis of gas-particle flow in a scaled circulating fluidized bed, Ph.D. thesis, University of Stavanger, Norway (2016).

[46] J. Kussin, M. Sommerfeld, Experimental studies on particle behaviour and turbulence modification in horizontal channel flow with different wall roughness, Experiments in Fluids 33 (2002) 143–159.

[47] C. Güttler, D. Heißelmann, J. Blum, S. Krijt, Normal collisions of spheres: A literature survey on available experiments, arXiv preprint arXiv:1204.0001 (2012).